Progress In Electromagnetics Research, Vol. 154, 65–78, 2015

Temperature-Dependent Electromagnetic Performance Predictions of a Hypersonic Streamlined Radome

Raveendranath U. Nair*, S. Vandana, S. Sandhya, and Rakesh M. Jha

Abstract—Nosecone radomes of hypersonic flight vehicles show degradation of electromagnetic (EM) performance characteristics due to variations in the dielectric parameters (dielectric constant and electric loss tangent) of the radome wall resulting from heating due to extreme aerodynamic drag. It is indicated that the EM performance predictions based on conventional monolithic half-wave wall based on average dielectric parameters corresponding to temperature ranges in hypersonic conditions may not be accurate. This necessitates the radome wall under hypersonic conditions to be modeled as an inhomogeneous dielectric structure for accurate EM performance predictions. In the present work, the hypersonic radome is considered as an *inhomogeneous dielectric radome* such that the cross-section of the radome wall in each EM window region is considered as an *inhomogeneous planar layer (IPL) model* with stacked layers of varying dielectric parameters. The material considered is RBSN Ceralloy 147-010F (an alloy of silicon nitride), which has excellent thermal shock resistance, dielectric and mechanical properties required for hypersonic radome applications. The EM modeling of a section of the radome wall in hypersonic conditions (i.e., IPL structure) is based on *Equivalent Transmission Line Method.* A comparative study of basic EM performance parameters of the radome wall (power transmission, power reflection, and insertion phase delay) for both the *IPL model* and conventional *monolithic half-wave model* are carried out over a range of incidence angles corresponding to the antenna scan ranges in each EM window region of the radome. Further the study is extended to compute the EM performance parameters of an actual tangent ogive nosecone radome (made of RBSN Ceralloy 147-010F) enclosing an X-band slotted waveguide planar array antenna, in a hypersonic environment. The antenna-radome interaction studies are based on 3-D *Ray tracing* in conjunction with *Aperture Integration Method.* It is observed that the EM performance analysis based on conventional monolithic radome wall design cannot accurately predict the radome performance parameters in actual operating conditions during hypersonic flight operations. The current work establishes the efficacy of *Inhomogeneous Dielectric Radome* model for better EM performance predictions of streamlined airborne radomes in hypersonic environments.

1. INTRODUCTION

During hypersonic flight operations (velocity > Mach 5), the temperature of the outer surface of the radome wall is much higher than that of inner surface due to extreme aerodynamic drag [1–4]. Under these conditions, the large temperature gradient existing across the radome wall results in variations in the dielectric parameters (dielectric constant and electric loss tangent) of the radome wall and hence radome EM performance parameters (Fig. 1). So the conventional design of radome wall configurations based on average dielectric parameters may not be accurate in EM performance predictions during hypersonic flight operations. In previously reported works, the boresight error characteristics of streamlined ceramic radomes were reported with the assumption of a linear temperature distribution

Received 26 May 2015, Accepted 27 October 2015, Scheduled 2 December 2015
* Corresponding author: Raveendranath Unnikrishnan Nair (raviunair@css.nal.res.in).
The authors are with the Centre for Electromagnetics, CSIR-National Aerospace Laboratories, Bangalore-560017, India.

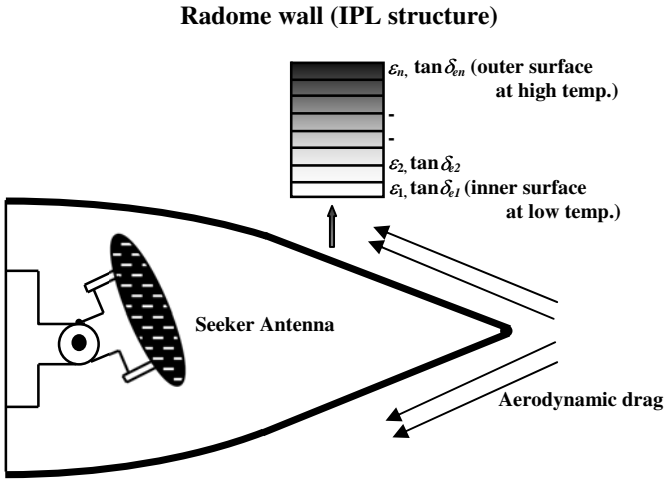

Figure 1. Streamlined nosecone radome under hypersonic conditions (inhomogeneous dielectric radome).

through the radome wall [5]. But this assumption is not valid in actual operating conditions in a hypersonic environment. The work reported in [6–8] regarding aerodynamic heating effects on EM performance parameters of missile radomes emphasized the need for better models for EM performance predictions. The temperature dependent radome EM performance predictions of a planar radome wall were reported by the authors elsewhere for analyzing the EM performance characteristics over a wide range of incidence angles [9]. In a recently reported work [10], the authors have presented the co-pol transmission and boresight error characteristics of a hypersonic radome considering the effect of temperature dependent dielectric parameters. As the dielectric properties have significant effect on the radome performance parameters, the temperature dependent EM performance predictions are in great demand for hypersonic airborne applications. For this purpose, antenna-radome interaction studies are carried out for the temperature dependent EM performance predictions of a streamlined nosecone radome made of RBSN Ceralloy 147-010F enclosing a seeker antenna operating at 10 GHz. RBSN Ceralloy 147-010F, an alloy of silicon nitride, is a promising ceramic radome material with excellent mechanical and dielectric properties, thermal shock resistance, and rain erosion/impact resistance required for hypersonic radome applications [11].

In Section 2, a planar slab of RBSN Ceralloy 147-010F in a hypersonic environment is modeled as inhomogeneous planar layer (IPL) structure based on *Equivalent Transmission Line Method*. Here the basic EM performance parameters (such as power transmission, power reflection, and insertion phase delay etc.) of the planar slab over a wide range of incidence angles (encountered in streamlined nosecone radome applications) corresponding to different *EM window regions* are computed using measured dielectric parameters of RBSN Ceralloy 147-010F [11]. A comparative study of basic EM performance parameters of conventional *Monolithic half-wave design* (*Monolithic Model*) and *IPL model* is also given in this section to indicate that the EM performance predictions for streamlined radomes in a hypersonic environment based on conventional "monolithic design" may not be accurate.

In Section 3, the EM performance predictions of an actual hypersonic streamlined nosecone radome (made of RBSN Ceralloy 147-010F), enclosing a highly directional seeker antenna (operating at 10 GHz with TE polarization), are carried out considering it as an "*Inhomogeneous Dielectric Radome*" with the radome wall as *IPL* structure. The antenna-radome interaction studies are performed based on 3-D *Raytracing* in conjunction with *Aperture Integration Method*. The EM performance parameters (co-pol transmission, cross-pol transmission, boresight errors etc.) of the nosecone radome are computed for different *EM window regions* corresponding to the antenna scan range. A comparative study of the EM performance parameters of conventional *Monolithic Half-wave Radome* and *Inhomogeneous Dielectric Radome* for different EM window regions is included in this section to establish its potential application for better EM performance predictions in a hypersonic environment.

2. IPL MODELING OF THE RADOME WALL

The EM window regions of the streamlined nosecone radome considered here, corresponding to antenna scan ranges, are represented by R_1, R_2, and R_3 (Fig. 2). Since the radome wall has to withstand very high temperatures ($> 1000°$C) in hypersonic flight operations, it is noted that the temperature corresponding to the surface (outer/inner) of the hypersonic radome vary non-linearly along the surface from radome nose-tip to radome base, and across the radome wall thickness. Hence the EM modeling of radome in hypersonic environment is quite complex. The altitude and velocity histories of the aerospace vehicle have to be used to predict the temperature profile due to aerodynamic heating effects. Table 1 shows the approximate temperature ranges existing across the radome wall in hypersonic environment corresponding to different EM window regions [5].

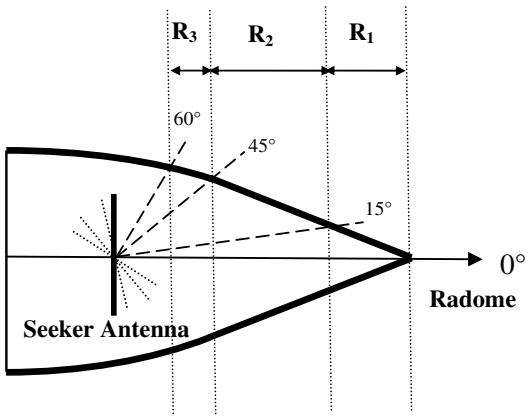

Figure 2. EM window regions of the hypersonic radome.

Table 1. Approximate temperature ranges across the hypersonic radome wall in EM window regions.

EM window region	Antenna scan range	Range of angle of Incidence	Approximate temperature range across the radome wall
R_1	0°–15°	50°–65°	860°C–1400°C
R_2	15°–45°	30°–55°	775°C–1300°C
R_3	45°–60°	0°–30°	240°C–775°C

Since the antenna is highly directional, the footprint of antenna beam on the surface of radome wall is quite small. So the temperature gradient along the intercept area of the antenna beam on the radome wall is assumed to be small as compared to that across the radome wall thickness. Hence the cross-section of the hypersonic radome wall in each EM window region can be considered as an *IPL structure*.

The dielectric parameters (ε_r and $\tan\delta_e$) of RBSN Ceralloy 147-010F are estimated over the temperature range 25°C–1400°C based on measured dielectric data [11] and are shown in Fig. 3. The total thickness of the RBSN Ceralloy 147-010F slab is taken as 7.13 mm, which is the optimized *half-wave wall thickness* at 10 GHz (antenna operating frequency) corresponding to maximum power transmission for TE polarization (or perpendicular polarization) at high incidence angle 65° for the streamlined radome considered in this work. For the estimation of the optimized wall thickness mentioned above, the average dielectric parameters ($\varepsilon_r = 5.235$; $\tan\delta_e = 0.0036$) of the material over the temperature range 200°C–1400°C (covering R_1, R_2, and R_3) are considered.

Large temperature gradient existing across the RBSN Ceralloy 147-010F radome wall in hypersonic conditions makes it an inhomogeneous planar layer (*IPL*) made up of stacked dielectric layers with

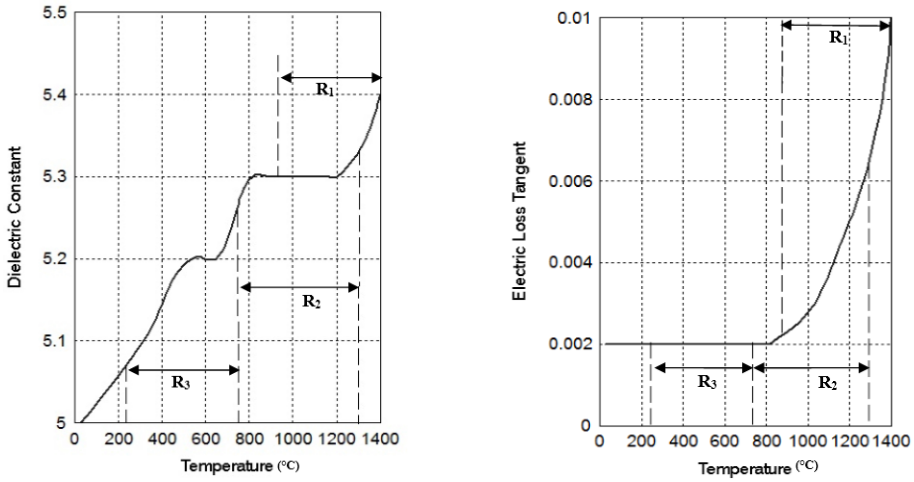

Figure 3. Variation of dielectric parameters of RBSN Ceralloy 147-010F with temperature (based on [11]). (a) Dielectric constant. (b) Electric loss tangent.

Table 2. Parameters of constitutive layers of IPL model of radome wall in window region R_1.

Layers of IPL wall	Average bulk temperature of the layer	Average dielectric constant (ε_r)	Average electric loss tangent ($\tan\delta_e$)	Location of boundaries of layers within the radome wall* (in mm)
Layer 1	940	5.30	0.0026	0–2.119
Layer 2	1093	5.30	0.0039	2.119–4.048
Layer 3	1215	5.30	0.0051	4.048–5.333
Layer 4	1267	5.32	0.0060	5.333–5.400
Layer 5	1276	5.33	0.0061	5.400–5.570
Layer 6	1288	5.33	0.0064	5.570–5.720
Layer 7	1298	5.34	0.0066	5.720–5.850
Layer 8	1310	5.35	0.0073	5.850–6.021
Layer 9	1322	5.35	0.0075	6.021–6.160
Layer 10	1333	5.36	0.0079	6.160–6.322
Layer 11	1344	5.36	0.0086	6.322–6.460
Layer 12	1355	5.37	0.0088	6.460–6.608
Layer 13	1366	5.38	0.0090	6.608–6.756
Layer 14	1377	5.38	0.0092	6.756–6.904
Layer 15	1388	5.39	0.0096	6.904–7.042
Layer 16	1397	5.40	0.0099	7.042–7.130

*The inner surface of IPL radome wall is considered as the reference plane.
0 mm — refers to the inner surface of IPL radome wall at low temp. 860°C in window R_1.
7.13 mm — refers to outer surface of IPL radome wall at high temp. 1400°C in window R_1.

varying temperature-dependent dielectric parameters (dielectric constant and electric loss tangent). The boundaries of dielectric layers of the IPL model of the radome wall corresponding to each EM window region are determined based on polynomial curve fitting based on temperature-dependent dielectric data of the material shown in Fig. 3. In window region R_1, 17 degree polynomial equation is employed for curve fitting across the radome wall to identify the boundaries. In Regions R_2 and R_3, 7 degree polynomial equation is used to determine the boundaries. In order to compute EM performance parameters, the dielectric parameters corresponding to the average bulk temperature of each layer of IPL wall in the given window region are estimated (Tables 2–4).

Table 3. Parameters of constitutive layers of IPL model of radome wall in window region R_2.

Layers of IPL wall	Average bulk temperature of the layer	Average dielectric constant (ε_r)	Average electric loss tangent ($\tan\delta_e$)	Location of boundaries of layers within the radome wall* (in mm)
Layer 1	808	5.30	0.0020	0–0.894
Layer 2	871	5.30	0.0021	0.894–1.704
Layer 3	942	5.30	0.0027	1.704–2.824
Layer 4	1026	5.30	0.0033	2.824–3.985
Layer 5	1153	5.30	0.0047	3.985–6.289
Layer 6	1269	5.33	0.0061	6.289–7.13

*The inner surface of IPL radome wall is considered as the reference plane.
0 mm — refers to the inner surface of IPL radome wall at low temp. 775°C in window R_2.
7.13 mm — refers to outer surface of IPL radome wall at high temp. 1300°C in window R_2.

Table 4. Parameters of constitutive layers of IPL model of radome wall in window region R_3.

Layers of IPL wall	Average bulk temperature of the layer	Average dielectric constant (ε_r)	Average electric loss tangent ($\tan\delta_e$)	Location of boundaries of layers within the radome wall* (in mm)
Layer 1	284	5.07	0.0020	0–1.188
Layer 2	373	5.12	0.0020	1.188–2.376
Layer 3	463	5.17	0.0020	2.376–3.564
Layer 4	552	5.20	0.0020	3.564–4.752
Layer 5	641	5.20	0.0020	4.752–5.940
Layer 6	730	5.24	0.0020	5.940–7.13

*The inner surface of IPL radome wall is considered as the reference plane.
0 mm — refers to the inner surface of IPL radome wall at low temp. 240°C in window R_3.
7.13 mm — refers to outer surface of IPL radome wall at high temp. 7750°C in window R_3.

In order to estimate the basic EM performance parameters mentioned above, *IPL* radome wall is considered as a multilayered structure with different sections corresponding to different dielectric layers (Fig. 4). As compared to the free space, different layers of IPL structure can be considered as low impedance lines connected end-to-end. Here '*Monolithic Model*' refers to the conventional monolithic

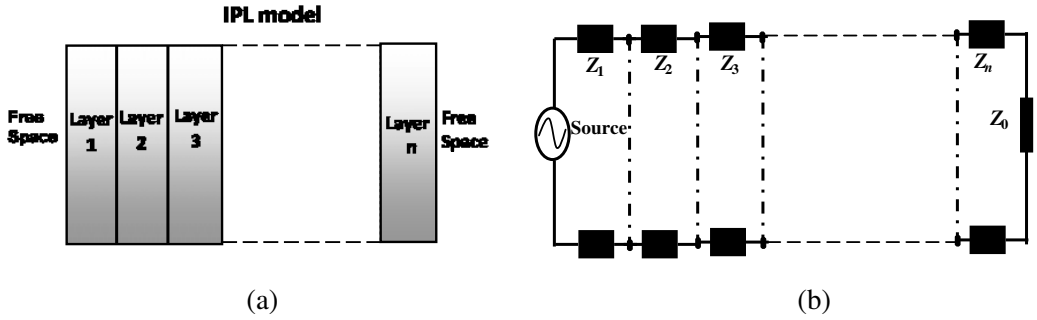

Figure 4. (a) *IPL* model of radome wall. (b) Equivalent circuit model of *IPL* radome wall.

half-wave radome wall design based on average dielectric parameters, whereas '*IPL Model*' refers to the radome wall of same material and thickness in actual operating conditions (i.e., in hypersonic environment) at high mach speed.

The EM performance parameters (transmission, reflection and insertion phase delay) of both IPL and monolithic slabs are computed based on *Equivalent Transmission Line Method* [4]. Here $Z_1, Z_2, \ldots, Z_n$ represent impedances of the respective layers and Z_0 is the characteristic impedance of free space. The A, B, C, D parameters of each layer depend on the EM material parameters of the respective layer, the thickness of the layer, the incidence angle, and the normalized impedance corresponding to the polarization (TE/TM) of incident wave.

The whole IPL structure can be represented by a single $ABCD$ matrix, obtained by the multiplication of matrices corresponding to individual layers. The voltage-current transmission matrix of the entire *IPL* radome wall is obtained as

$$\begin{bmatrix} A & B \\ C & D \end{bmatrix} = \begin{bmatrix} \cos\phi_1 & j\dfrac{Z_1}{Z_0}\sin\phi_1 \\ j\dfrac{Z_0}{Z_1}\sin\phi_1 & \cos\phi_1 \end{bmatrix} \begin{bmatrix} \cos\phi_2 & j\dfrac{Z_2}{Z_0}\sin\phi_2 \\ j\dfrac{Z_0}{Z_2}\sin\phi_2 & \cos\phi_2 \end{bmatrix} \cdots \begin{bmatrix} \cos\phi_i & j\dfrac{Z_i}{Z_0}\sin\phi_i \\ j\dfrac{Z_0}{Z_i}\sin\phi_i & \cos\phi_i \end{bmatrix} \cdots \begin{bmatrix} \cos\phi_n & j\dfrac{Z_n}{Z_0}\sin\phi_n \\ j\dfrac{Z_0}{Z_n}\sin\phi_n & \cos\phi_n \end{bmatrix} \tag{1}$$

where ϕ_i is the electrical length corresponding to the ith layer of IPL wall. It is a function of the complex permittivity, ε_i^* of the ith layer, the angle of incidence at the ith layer θ_i, and the thickness of the ith layer d_i.

The power transmission coefficient is expressed as

$$P_t = \frac{4}{(A+B+C+D)^2} \tag{2}$$

The power reflection coefficient is expressed as

$$P_r = \left(\frac{A+B-C-D}{A+B+C+D}\right)^2 \tag{3}$$

The phase distortions due to IPL wall is represented by the insertion phase delay and it is represented by

$$\begin{aligned} IPD \;=\; & -(\angle T_1 + \angle T_2 + \ldots + \angle T_i \ldots + \angle T_n) \\ & -\frac{2\pi}{\lambda}\left(d_1\cos\theta_1 + d_2\cos\theta_2 + \ldots + d_i\cos\theta_i + \ldots + d_n\cos\theta_n\right) \end{aligned} \tag{4}$$

Here $\angle T_1, \angle T_2, \angle T_i, \ldots, \angle T_n$ are the phase angles associated with the voltage transmission coefficients of the layers with thicknesses $d_1, d_2, \ldots, d_n$ respectively. $\theta_1, \theta_2, \ldots, \theta_n$ are the corresponding incidence angles at the boundaries of the constitutive layers.

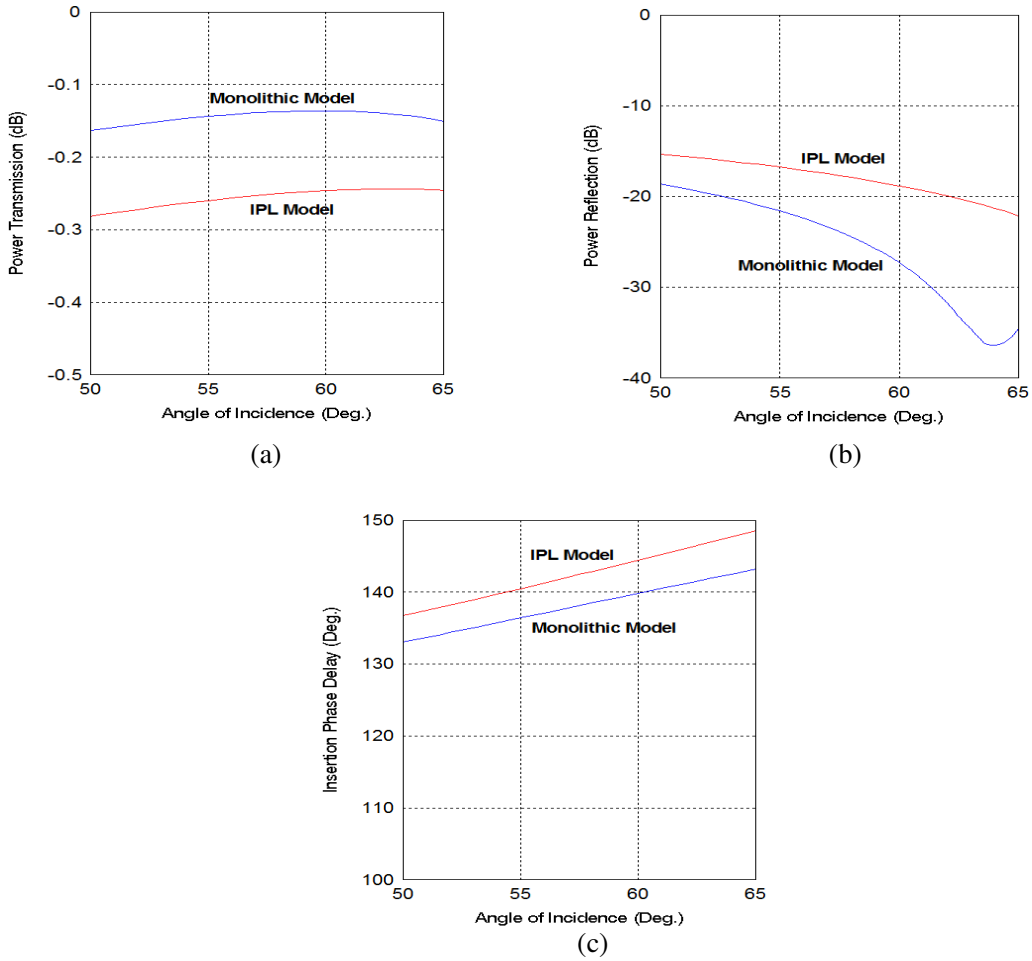

Figure 5. (a) Power transmission, (b) power reflection, and (c) insertion phase delay corresponding to window region R_1 ('IPL Model' refers to slab of radome wall in hypersonic environment; 'Monolithic Model' refers to slab of monolithic radome wall based on average dielectric parameters).

The power transmission, power reflection, and insertion phase delay parameters of both *IPL Model* and *Monolithic Model* of RBSN Ceralloy 147-010F at 10 GHz for TE polarization (same as that of antenna polarization) are computed over the given range of incidence angles corresponding to window regions R_1, R_2, and R_3 and are shown in Figs. 5–7.

The parameters of *IPL Model* for EM window R_1 are given in Table 2. The power transmission of IPL slab is less than that of monolithic slab over the entire range of incidence angles, which is attributed to the impedance mismatching due to variations in dielectric loss across the IPL slab (shown in Fig. 5(a)). A local minimum is observed for power reflection characteristics around 64°. Since there is no drastic variation in power transmission as seen in Fig. 5(a), the reduction in power reflection for "Monolithic Model" is attributed due to localized absorption. The reduction in the transmission efficiency of radome wall will affect the radar range. The power reflection of IPL slab is high compared to monolithic slab (shown in Fig. 5(b)).

This will cause degradation of antenna radiation pattern resulting in sidelobe level (SLL) degradations and emergence of flash lobes. However, the insertion phase delay of IPL slab does not show much variation compared to monolithic slab (shown in Fig. 5(c)).

The parameters of *IPL Model* for window region R_2 are given in Table 3. The power transmission of IPL slab is low compared to monolithic slab for region R_2 also. The power reflection of IPL slab is high as compared to monolithic slab (shown in Fig. 6(b)). In region R_2 also, the insertion phase delay of IPL slab does not show much variation from that of monolithic slab.

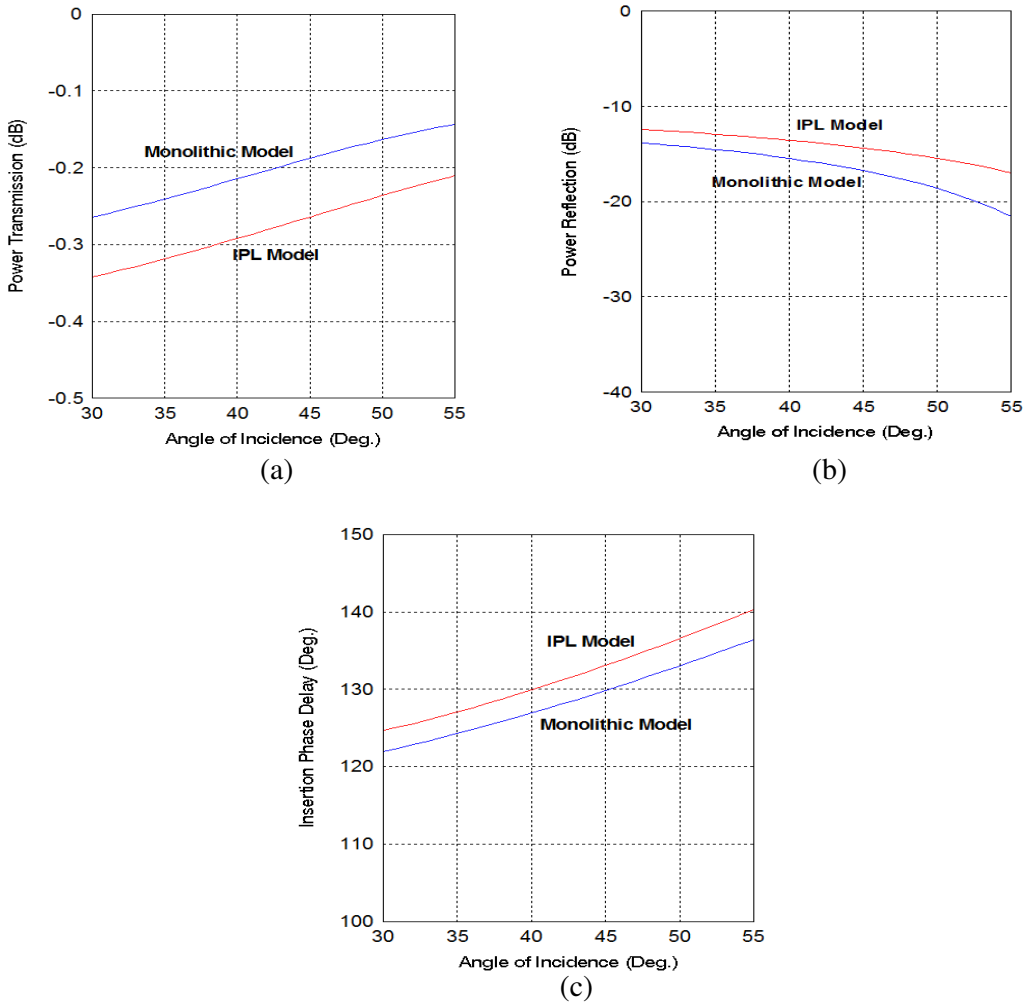

Figure 6. (a) Power transmission, (b) power reflection and (c) insertion phase delay corresponding to window region R_2 ('IPL Model' refers to slab of radome wall in hypersonic environment; 'Monolithic Model' refers to slab of monolithic radome wall based on average dielectric parameters).

For window region R_3, the parameters of *IPL Model* are given in Table 4. The EM performance characteristics of window region R_3 are shown in Fig. 7. The power transmission of IPL slab is high compared to monolithic slab in region R_3 which indicates better impedance matching at these incidence angles. However, power reflection and insertion phase delay characteristics of IPL slab do not show much variation as compared to monolithic slab.

The study shows that the EM performance characteristics of *Monolithic Model* with optimized wall thickness based on average dielectric parameters over the temperature range are different from that of *IPL Model*. This indicates that 'IPL Model' is more realistic as compared to 'Monolithic Model' as it incorporates temperature-dependent variation of dielectric parameters. For electrically large radomes, the radome wall is considered as locally flat at the point of intersection of the ray (emanating from the antenna) with the radome surface. Further, the thickness of the "flat section" at the ray-radome intersection region is assumed to be same as that of the radome wall at the intersection point.

This study will facilitate to assess the variations of power transmission, power reflection, and insertion phase delay due to the large temperature gradient existing across the slab like section of radome wall made of RBSN Ceralloy 147-010F. Further, the present work indicates that the EM performance predictions of the streamlined airborne radomes based on conventional *Monolithic Model* may not be applicable in actual operating conditions in a hypersonic environment. In view of this, EM performance

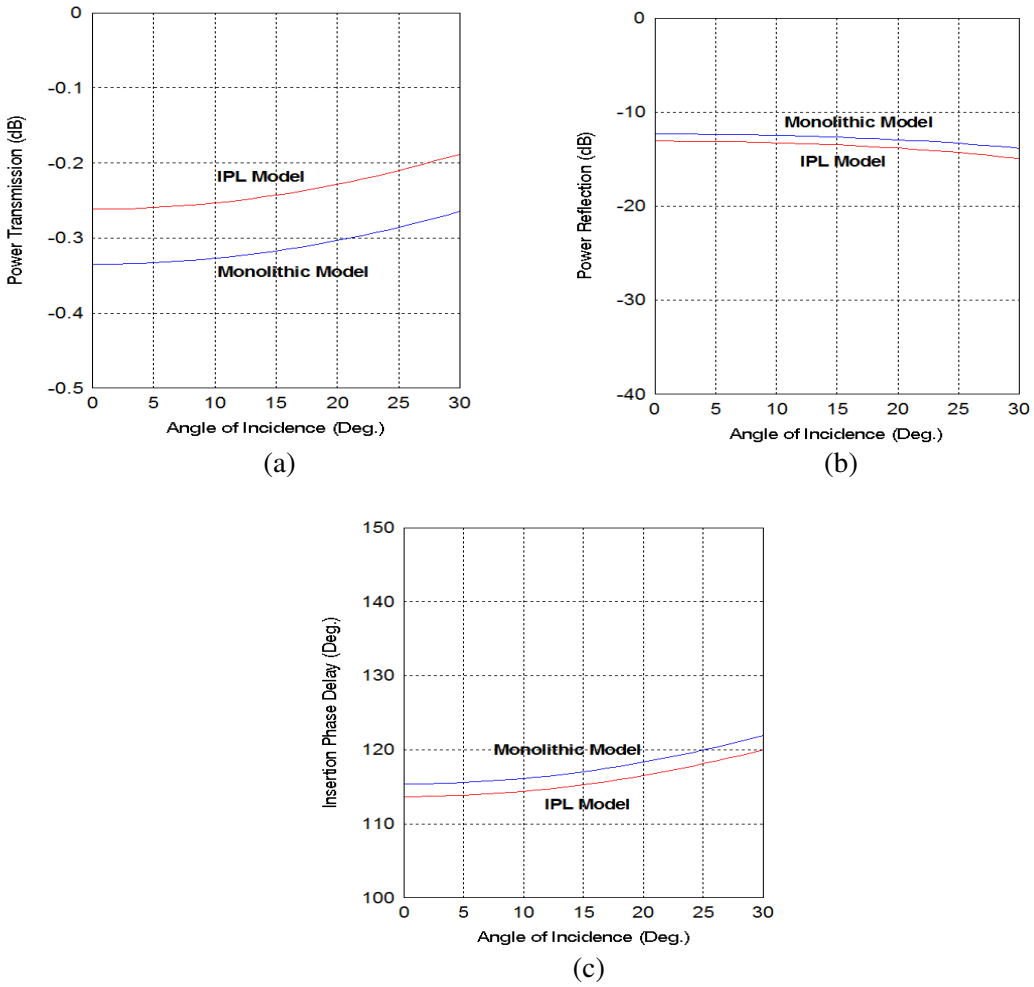

Figure 7. (a) Power transmission, (b) power reflection and (c) insertion phase delay corresponding to window region R_3 ('IPL Model' refers to slab of radome wall in hypersonic environment; 'Monolithic Model' refers to slab of monolithic radome wall based on average dielectric parameters).

predictions in such environment are carried out for a tangent ogive nosecone radome made of RBSN Ceralloy 147-010F based on *IPL Model* of radome wall.

3. EM PERFORMANCE PREDICTIONS OF ANTENNA-RADOME SYSTEM IN HYPERSONIC ENVIRONMENT

The tangent ogive nosecone radome made of RBSN Ceralloy 147-010F (height = 400 mm; base diameter = 200 mm; and wall thickness = 7.13 mm) encloses a monopulse slotted waveguide planar array antenna located at a distance of 80 mm from the radome base (diameter = 120 mm) and operating at 10 GHz with cosine aperture distribution and TE polarization. The azimuth and elevation antenna scan ranges are $\pm 60^{\circ}$ respectively. The interaction of the slotted waveguide planar array antenna with the radome is carried out by a 3D *Ray-tracing* procedure in conjunction with *Aperture Integration* method [12, 13]. The EM performance parameters of the radome are computed by considering the *antenna-radome system w.r.t.* the *antenna alone* reference. The procedure for EM performance analysis of antenna-radome system includes: (i) fixing of radome coordinates, (ii) determination of the space phase terms of antenna far-field, along with its transformation to the radome coordinates, and (iii) obtaining radome EM performance parameters of the radome (e.g., Co-pol power transmission, X-pol, BSE etc.) as a function of antenna scan angle. For the antenna-radome system considered, the normalized array

pattern is given by [13]

$$E_{AR} = \frac{\sum_{m=1}^{M}\sum_{n=1}^{N} F_{mn}^{a} T_{mn} e^{-j(k_x x + k_y y + k_z z)}}{\sum_{m=1}^{M}\sum_{n=1}^{N} F_{mn}^{a}} \tag{5}$$

where T_{mn} and F_{mn}^{a} are the transmission coefficient and aperture distribution for the mnth radiating slot on antenna plate respectively. The *aperture distribution characteristics* of the rectangular slots of the antenna are incorporated in the computation of radome performance parameters. Using (5), the sum port voltage is estimated for each antenna scan angle. The sum port voltages obtained are used for the computation of co-pol and cross-pol transmission parameters of the radome.

Let ΔV_{Az} and ΔV_{El} be the respective receiving port voltages corresponding to azimuth and elevation difference channels for the monopulse antenna. These voltages are determined for the given pattern look direction using (5). The boresight errors for azimuth and elevation scans are given by [14, 15]

$$BSE_{Az} = \frac{\Delta V_{Az}}{K_{Az}} \tag{6}$$

$$BSE_{El} = \frac{\Delta V_{El}}{K_{El}} \tag{7}$$

Here K indicates the monopulse antenna sensitivity, which depends on the difference channel port voltages and azimuth/elevation offsets. The EM performance parameters (Co-pol power transmission, X-pol transmission, boresight error (BSE) etc.) of antenna-radome system are computed for antenna scan angles corresponding to window regions R_1, R_2, and R_3 based on 3D *Ray-tracing* procedure in conjunction with *Aperture Integration* method. Here the tangent ogive radome structure based on *Monolithic Model* and *IPL Model* are referred as *Monolithic Radome* and *Inhomogeneous Dielectric Radome*, respectively.

3.1. EM Performance Predictions in Window Region R_1

The window region R_1 is considered as "critical nose-cone sector" as the radome performance parameters degrade drastically due to (i) extreme aerodynamic conditions, and (ii) high incidence angles encountered by the antenna beam. The angle of incidence is maximum when the antenna beam is pointing along the radome axis and it decreases with increase in antenna scan angle. For the antenna-radome system considered in the present work, the angle of incidence is varying from 50°–65° in R_1.

Figures 8(a)–(d) show the EM performance characteristics of the radome in the window region R_1. The co-pol power transmission is low for *Inhomogeneous Dielectric Radome* as compared to that

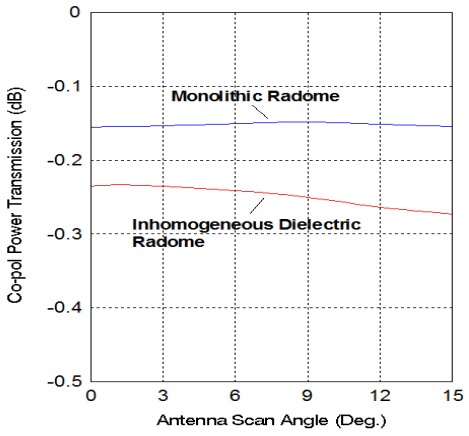

(a)

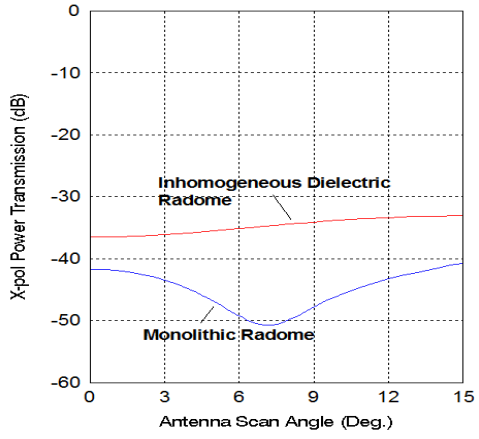

(b)

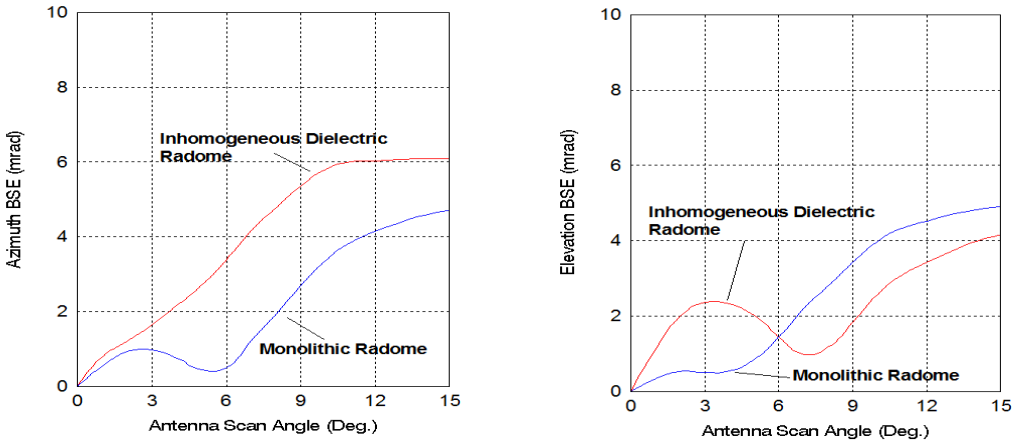

Figure 8. (a) Co-pol power transmission characteristics in Window Region R_1. (b) X-pol power transmission characteristics in Window Region R_1. (c) Azimuth BSE characteristics in Window Region R_1. (d) Elevation BSE characteristics in Window Region R_1.

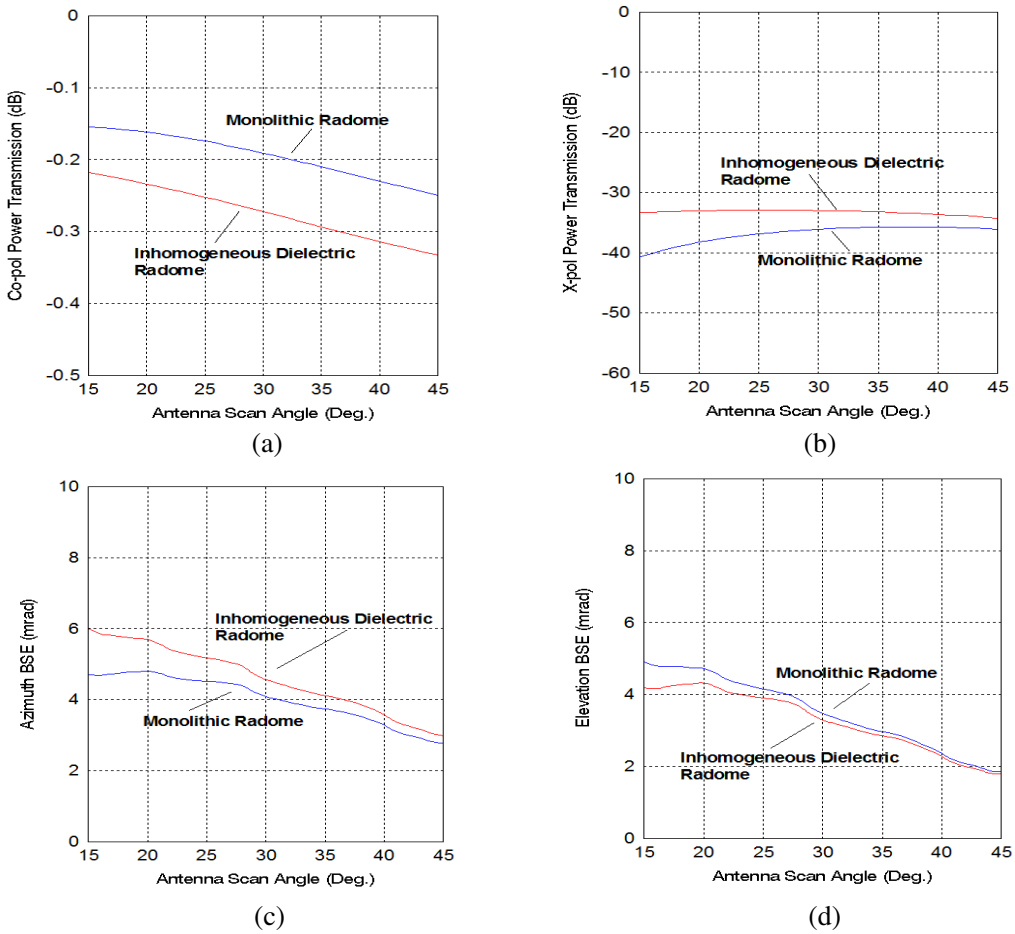

Figure 9. (a) Co-pol power transmission characteristics in Window Region R_2. (b) X-pol power transmission characteristics in Window Region R_2. (c) Azimuth BSE characteristics in Window Region R_2. (d) Elevation BSE characteristics in Window Region R_2.

of *Monolithic Radome*. Regarding cross-pol characteristics, it is well above −40 dB for *Inhomogeneous Dielectric Radome*, which is undesirable for radar applications. For cross-pol transmission characteristics (shown in Fig. 8(b)) in Region R_1, the local minimum at the antenna scan angle 7° corresponds to cross-pol value −50.69 dB. Further, it is observed that the co-pol power transmission shows a gradual increase from −0.156 dB at 0° to −0.148 dB at 9° and thereafter it remains almost constant upto 15° in Region R_1. The local minimum is attributed due to the better impedance matching of radome wall to the incident wave in this antenna scan range. The azimuth boresight error of *Inhomogeneous Dielectric Radome* is higher than that of *Monolithic Radome* in the antenna scan range 0°–15°. However, the elevation boresight error of *Inhomogeneous Dielectric Radome* is higher than that of *Monolithic Radome* only in the scan range 0°–6° in region R_1.

3.2. EM Performance Predictions in Window Region R_2

The EM performance characteristics of the radome in the window region R_2 are shown in Figs. 9(a)–(d). The angle of incidence is varying from 30°–55° corresponding to the antenna scan range in R_2.

The co-pol power transmission of *IPL Model* shows considerable degradation as compared to monolithic case. As in the window region R_1, the cross-pol level of IPL is higher than that of monolithic. Azimuth boresight error of *IPL Model* is higher than that of *Monolithic Model,* while elevation boresight error of *IPL Model* is less than that of *Monolithic Model*.

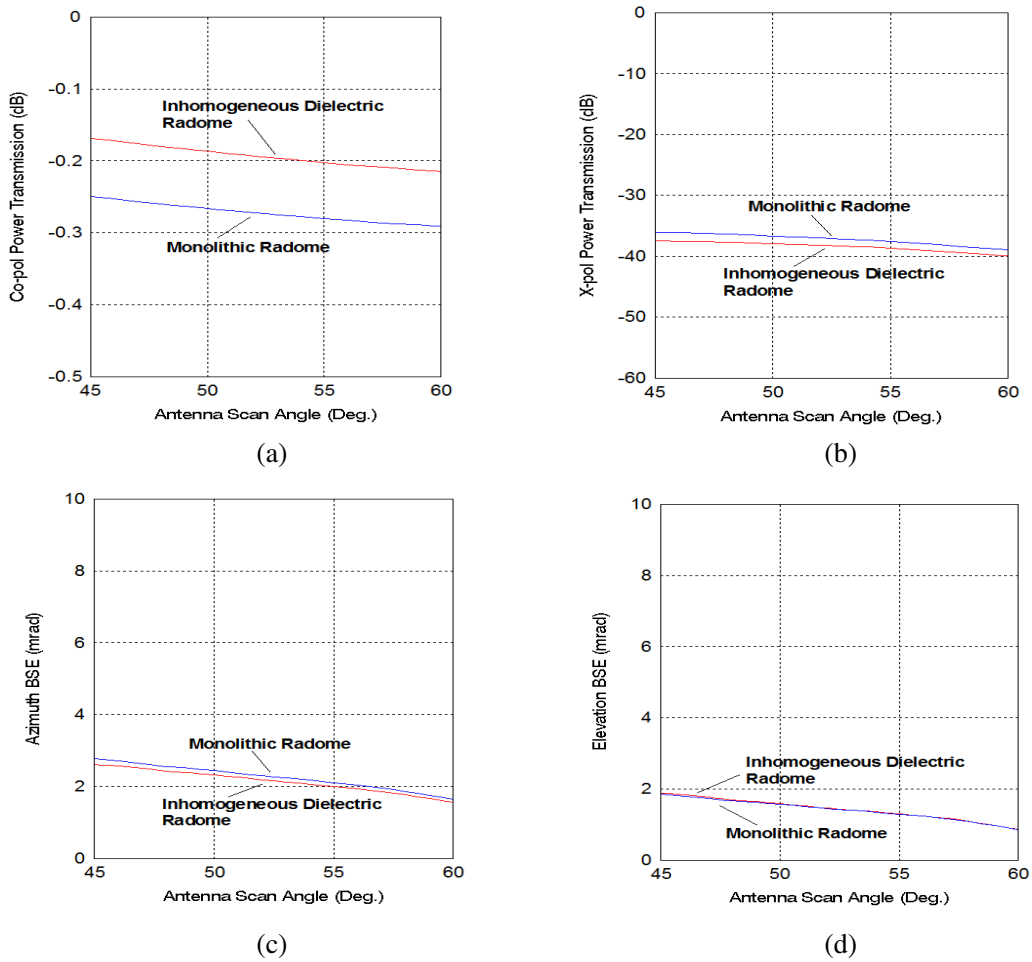

Figure 10. (a) Co-pol power transmission characteristics in Window Region R_3. (b) X-pol power transmission characteristics in Window Region R_3. (c) Azimuth BSE characteristics in Window Region R_3. (d) Elevation BSE characteristics in Window Region R_3.

3.3. EM Performance Predictions in Window Region R_3

Figures 10(a)–(d) show the radome EM performance characteristics corresponding to window region R_3. In this scan range, the angle of incidence is varying from 0°–30°. It is noted that the angle of incidence up to 30° can be considered as near-normal incidence case. Hence the variations in EM performance parameters may be minimal in this sector of the radome.

Contrary to the window regions R_1 and R_2, the co-pol power transmission of *IPL Model* in window region R_3 is better than that of *Monolithic Model* as shown in Fig. 10(a). This is due to better impedance matching of *IPL Model*. However, the other performance parameters (cross-pol and boresight errors) of IPL radome do not show much variation from that of monolithic case.

4. CONCLUSION

The potential application of *Inhomogeneous Dielectric Radome* model for the temperature-dependent EM performance predictions of a hypersonic streamlined airborne radome (made of RBSN Ceralloy 147-010F) is presented. It is noted that the measurement of EM performance parameters of a hypersonic radome in actual operating conditions is not yet practically realized, as full-scale radome EM performance tests in simulated environments (like wind-tunnel facility, microwave anechoic chamber with sudden expansion burners [8], etc.) are cumbersome and not feasible. In this regard, the EM performance analysis presented here establishes the efficacy of *Inhomogeneous Dielectric Radome* model (based on measured dielectric data of radome material over the temperature profile in hypersonic conditions) as compared to conventional *Monolithic Radome* model, for better EM performance predictions of hypersonic streamlined nosecone radomes.

However, plasma sheath formation in hypersonic flight operations is not considered in the current work since the thickness and density of the plasma sheath depends on velocity and altitude of hypersonic vehicle, which makes it difficult to incorporate in EM modeling. Since the present work is based on "bare radome", it will facilitate the radome designer to fine-tune the thickness of bare radome wall so that the thickness of (i) radome paint, (ii) hermetic coating for protection from moisture absorption, and (iii) thermal insulation coating on the inner radome surface to protect the seeker antenna from heat flow, can be properly selected. Further, simulation results for BSE can be implemented in HWIL (hardware-in-loop) auto correction system of airborne radar system for BSE correction.

REFERENCES

1. Poisl, W. H., C. Solecki, and J. M. Wahl, "Mission challenges spur next generation missile radome materials innovations," *Raytheon Technology Today*, No. 2, 64–65, May 2012.
2. Chen, F., Q. Shen, and L. Zhang, "Electromagnetic optimal design and preparation of broadband ceramic radome material with graded porous structure," *Progress In Electromagnetics Research*, Vol. 105, 445–461, 2010.
3. Zhou, L., Y. Pei, R. Zhang, and D. Fang, "Optimal design for high-temperature broadband radome wall with symmetrical graded porous structure," *Progress In Electromagnetics Research*, Vol. 127, 1–14, 2012.
4. Nair, R. U. and R. M. Jha, "Electromagnetic design and performance analysis of airborne radomes: Trends and perspectives," *IEEE Antennas and Propagation Magazine*, Vol. 56, 276–298, August 2014.
5. Kilcoyne, N. R., "A two-dimensional ray-tracing method for the calculation of radome boresight error and antenna pattern distortion," Technical Report: 2767-2, Electro Science Laboratory, Department of Electrical Engineering, The Ohio State University, Columbus, Ohio, USA, October 1969.
6. Weckesser, L. B., R. K. Frazer, D. J. Yost, B. E. Kuehne, G. P. Tricoles, R. Hayward, and E. L. Rope, "Aerodynamic heating effects on radome boresight errors," *Proceeding of 14th Symposium on Electromagnetic Windows*, 45–51, Atlanta, June 1978.

7. Pendergrass, N. S., "Radome analysis," Technical Report: SD83-BMDSCOM-2682, Department of the Army, Ballistic Missile Defence Command, Systems Technology Project Office, Huntsville, Alabama, USA, October 1983.
8. Rope, E. L. and G. Tricoles, "Feasibility of electromagnetic tests of radomes heated by hot gases," *Proceeding of IEEE Antennas and Propagation Society International Symposium*, Vol. 2, 879–880, June 1986.
9. Parul, R. U. Nair, and R. M. Jha, "Temperature dependent EM performance predictions of dielectric slab based on inhomogeneous planar layer model," *Proceeding of IEEE International Symposium on Antennas and Propagation*, 1–2, Chicago, USA, July 2012.
10. Nair, R. U., S. Sandhya, and R. M. Jha, "EM performance analysis of a hypersonic radome," *Proceeding of International Symposium on Antennas and Propagation (APSYM)*, 343–346, Cochin University of Science and Technology, Kochi, December 17–19, 2014.
11. Mangles, J., B. Mikijelji, and B. Lockhart, "Ceramic radomes for tactical missile systems," www.ceradyne-thermo.com.
12. Nair, R. U. and R. M. Jha, "Electromagnetic performance analysis of a novel monolithic radome for airborne applications," *IEEE Transactions on Antennas and Propagation*, Vol. 57, No. 11, 3664–3668, November 2009.
13. Kozakoff, D. J., *Analysis of Radome Enclosed Antennas*, Artech House, Norwood, USA, 2010.
14. Siwiak, K., A. Hessel, and L. R. Lewis, "Boresight errors induced by missile radomes," *IEEE Transactions on Antennas and Propagation,* Vol. 27, No. 6, 832–841, November 1979.
15. Burks, D. G., E. R. Graf, and M. D. Fahey, "A high-frequency analysis of radome-induced radar pointing error," *IEEE Transactions on Antennas and Propagation*, Vol. 30, No. 5, 947–955, September 1982.